Research Article

Check for updates

Cavitation evolution and damage by liquid nitrogen in a globe valve

Xia ZHOU[1], Xiao-qin ZHI[1,2✉], Xu GAO[2], Hong CHEN[2], Shao-long ZHU[1], Kai WANG[1], Li-min QIU[1], Xiao-bin ZHANG[1]

[1]*Institute of Refrigeration and Cryogenics, Zhejiang University, Hangzhou 310027, China*
[2]*State Key Laboratory of Technologies in Space Cryogenic Propellants, Beijing 100028, China*

Abstract: Valves are key components of the safety of fluid transportation systems because of induced disturbance and cavitation damage in them. In this study, a 2D model of a cryogenic globe valve with liquid nitrogen (LN_2) as working fluid was established by Fluent, and thermal effects were specially considered in the simulation. The validity of the LN_2 cavitation model was verified by the experimental data of hydrofoil LN_2 cavitation from earlier studies by NASA. Cavitation characteristics of LN_2 in the cryogenic globe valve under three typical working conditions were investigated. The average pressure and pressure pulse at different positions of the wall were further studied to reveal cavitation risks from fatigue and vibration. Results show that with similar valve structure and openings, the pressure pulsation frequencies of LN_2 are lower than those of water, and the shape and location of the cavitation clouds also show significant differences. For LN_2 cavitation, an extended period of valve opening at 66% should be avoided since its pressure pulse peak is the largest compared to openings of 33% and 100%, and reaches 5×10^7 Pa. The opening of 33% should also be monitored because of the large torque caused by the pressure difference between the two sides of the valve baffles. To prevent resonance, a critical state for the valve opening and the connecting pipe length is proposed. These predictions of cryogenic cavitation in the globe valve are helpful for the safe and reliable operation of cryogenic fluid transport systems.

Key words: Cavitation; Thermal effect; Cryogenic liquids; Cryogenic globe valve

1 Introduction

Fluid transportation system reliability is highly affected by flow stability since unsteady flow may lead to leakage in the pipeline and, in serious cases, even result in major system failure and safety incidents (Miwa et al., 2015). Valves are the key components affecting pipeline system safety due to their frequent change of operating mode and the induced disturbance to the flows. Especially, cavitation has a strong impact on the valve body, causing noise, vibration, and damage, and even affecting the normal operation of other components in the pipeline system (Chern et al., 2013; Zhu et al., 2019). Therefore, research on valve cavitation is of great importance for pipeline system operation.

✉ Xiao-qin ZHI, xiaoqin628@126.com

Ⓓ Xia ZHOU, https://orcid.org/0000-0003-4174-0745
   Xiao-qin ZHI, https://orcid.org/0000-0001-5369-9108

Recent studies of valve cavitation have indicated concerns. Saito et al. (2007) simulated the cavitation flow of the pump hydrofoil and cage-type valve with the 2D unsteady Navier-Stokes model of water. The cavitation features were provided. The sharp and high amplitude pressure pulses caused by bubble generation and collapse were captured. Amirante et al. (2014) performed experiments to estimate the effect of cavitation on the performance curves of a proportional valve with liquid oil. A 3D model was established to analyze the characteristics of cavitation that could not be experimentally evaluated. The low-pressure chamber and specifically the metering section, were the places where vapor cavitation occurred. Tabrizi et al. (2014) compared the flow patterns under several opening angles of a ball valve of water by computational fluid dynamics (CFD) simulation. It was found that the cavitation regions were located in the recirculation area with low-pressure of the ball valve. The cavitation index was calculated and the critical conditions for cavitation inception were revealed. Valdes et al. (2014)

conducted experiments on cavitation in a ball check valve with a typical brake liquid. The results were in good agreement with simulation. The flow coefficient was further deduced as a function of the Reynolds number and the cavitation number.

Considering the effects of structural parameters and boundary conditions on cavitation, the CFD simulation of water in a globe valve by Jin et al. (2018) showed that large bending radius, deviation distance, arc curvature, and small inlet velocity could limit the intensity of cavitation. Another research of Jin et al. (2020), with a sleeve regulating valve, investigated in detail the effects of valve core shapes on cavitation flows and found that cavitation intensities of ellipsoid and cylinder valve cores were greater than those of circular and truncated cone valve cores. The CFD simulation by Gholami et al. (2015) showed that the increase of the camber angle of the vanes to more than 70° could significantly reduce cavitation intensity, but would also cause a reduction in flow coefficient and increase in the cost of energy use.

For valve shape optimization, Palau-Salvador et al. (2008) numerically optimized the valve geometry by simplifying the piston geometry, the piston path and steps in the downstream chamber of the piston control valve with water as working fluid. The simulation results of a 40-A three-way reversing globe valve by Lee et al. (2016) showed that the cavitation effect of water could be reduced when both the waist length and the tail length were increased. The optimal size of the bottom plug was 6.50 mm for waist length and 6.69 mm for tail length, under which the percentage of cavitation could be minimized to 27%. Ko and Song (2015) proposed that the ratio of the narrowest gap area to the inlet area should be increased and the narrow gap length should be reduced to minimize oil cavitation in the solenoid valve. The optimal geometry design presented a maximum vapor volume fraction reduction from 0.740 to 0.051.

For cavitation and vibration, Kumagai et al. (2016) carried out a series of high-speed visualization experiments with oil. It was revealed that the vibration of the poppet valve was caused by the fluctuation of cavitation bubbles and the behavior of the annular vortex. A visualization experiment conducted by Yi et al. (2015), with valve housing fabricated in Perspex, indicated that the decrease of flow coefficient and fluid viscosity caused by oil cavitation will result in a reduced vibration frequency. It was also observed that the poppet vibration led to a dramatic increase of cavitation noise, because the vibration caused a quick and violent collapse of the numerous cavities developed in the throttling region.

The above research on valve cavitation has greatly improved the design and operation of valves in pipeline systems. However, these studies have mainly focused on the working fluids of water, oil, and other normal temperature liquids; cryogenic liquids were seldom involved. Liquid oxygen (LO_2), liquid nitrogen (LN_2), liquid hydrogen (LH_2), and other cryogenic liquids are significant in modern industry and in medical and aerospace fields (Steckelmacher, 1994; Zhang et al., 2014). Drastic vibration in the pipelines of these cryogenic fluids has become a significant safety risk for transportation systems.

Because of the great differences in physical properties and working conditions of cryogenic liquids and normal temperature liquids, cryogenic cavitation implies more complex mechanisms. The investigation of the cavitation in a convergent-divergent nozzle with both experimental and numerical methods by Giorgi et al. (2010) showed great differences in pressure amplitude and frequency between LN_2 and water. Under the usual working temperatures of LN_2 (77 K) and water (293 K), the saturated vapor pressure of LN_2 (97 152 Pa) is much larger than that of water (2333 Pa). Therefore, LN_2 is more likely to cavitate when throttling occurs. The liquid-gas density ratios of LN_2 and water are 175 and 58 151, respectively, which means much more LN_2 is needed than water to produce the same volume of gas. Moreover, the thermal conductivity, special heat capacity, and surface tension of LN_2 are quite different from those of water, which leads to a different temperature drop, bubble collapse, and instantaneous pressures of the cavitation characteristics. These discrepancies will be specifically explained in this research.

Although some research on cryogenic cavitation has been carried out and simple structures such as nozzles (Xue et al., 2019; Chen et al., 2021), hydrofoils (Zhu et al., 2016; Li et al., 2020; Xu et al., 2020), and pipes (Ishimoto and Kamijo, 2004; Lei et al., 2018; Yu et al., 2019) are involved, specific discussions about cryogenic valves are rather few and have only appeared in the last two years (Pinho et al., 2019; Lin et al., 2021). However, the influence of

thermal effects on valve cavitation has not been considered in valve cavitation simulations. Therefore, it is necessary to investigate the cryogenic valve cavitation with a thermal model, which illuminates cavitation induced instability problems in cryogenic liquid transportation systems.

In present study, the cavitation induced in the cryogenic globe valve was investigated by CFD simulation with a thermal effect involved, taking the common cryogenic fluid LN_2 as the working fluid. The cavitation characteristics of LN_2 under different openings were studied. The pulse pressure and average pressure on the valve wall were analyzed for their cavitation impact under different openings. The natural frequencies of the valve with different lengths of the connecting pipes were further investigated and compared with the fluid pulsation frequencies to prevent vibration resonance.

2 Numerical model

2.1 Geometry and mesh model

The short-shaft cryogenic globe valve is the most commonly used component in a cryogenic liquid transportation system. Fig. 1 shows a sketch diagram of a typical cryogenic globe valve (Jin et al., 2018). It shows the valve upstream part, the valve body (valve baffle, valve stem, valve seat, valve throat, valve core, and valve chamber), and the valve downstream part. A 2D valve physical model was established and the throttle cavitation effect of the valve throat and the subsequent flow development of the gas-liquid two-phase fluid are specially investigated. In order to make the calculation results more realistic, the computational domain includes the valve upstream and downstream connecting pipes to a length of 10D (pipe diameter $D=$ 50 mm). H is the displacement of the valve core, which also stands for the valve opening. Other parameters are the valve length $L=230$ mm, arc radius $R_1=80$ mm, $R_2=80$ mm, and the thickness of the valve core $T_{core}=$ 10 mm. The structure and partial enlargement of the model are as shown in Fig. 2, and the grids of the boundary layer near the wall are refined. Besides, due to the irregular and sharp shape of the valve baffle which leads to a low-quality mesh, simplifying the baffle size has little effect on the fluid flow direction of the mainstream fluid and basically does not affect

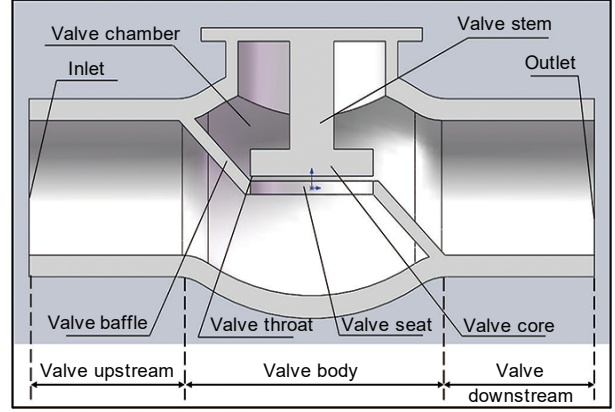the intensity of cavitation. The baffle size is thus simplified as a thin wall in the model.

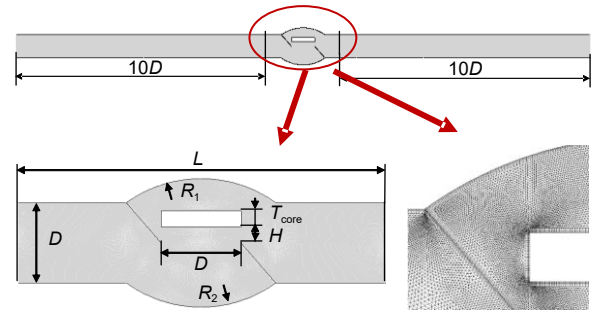**Fig. 1 Schematic structure of the cryogenic globe valve**

Fig. 2 Two-dimensional model of the cryogenic globe valve

2.2 Governing equations

Cavitation would cause the local temperature drop in the liquid, which will in return affect the cavitation development. Compared with the previous simulations of valves, thermal effect was considered in this study, that is, the energy equation was added to the simulation for temperature calculation. The mass continuity, and momentum and energy equations are given below (Comini and Del Giudice, 1985):

$$\frac{\partial}{\partial t}\left(\rho_m\right) + \frac{\partial}{\partial x_j}\left(\rho_m u_j\right) = 0, \quad (1)$$

$$\frac{\partial}{\partial t}\left(\rho_m u_i\right) + \frac{\partial}{\partial x_j}\left(\rho_m u_i u_j\right) = -\frac{\partial P}{\partial x_i} + \frac{\partial}{\partial x_j}\left[\left(\mu_m + \mu_t\right)\left(\frac{\partial u_i}{\partial x_j} + \frac{\partial u_j}{\partial x_i} - \frac{2}{3}\frac{\partial u_k}{\partial x_k}\delta_{ij}\right)\right], \quad (2)$$

$$\frac{\partial}{\partial t}\left(\rho_{\mathrm{m}}E\right) + \frac{\partial}{\partial x_j}\left[\left(\rho_{\mathrm{m}}E+P\right)u_j\right] = \\ \frac{\partial}{\partial x_j}\left(\lambda_{\mathrm{eff}}\frac{\partial T}{\partial x_j}\right) - h_{\mathrm{lat}}R. \tag{3}$$

In the above equations, ρ, u, μ, δ, λ, t, P, E, T, and R represented the density, velocity, viscosity, stress term, thermal conductivity, time, pressure, energy, temperature, and mass transfer rate per unit volume, respectively. x_i, x_j, and x_k denote the coordinate axes. λ_{eff} is the effective thermal conductivity. The subscripts m and t represent mixture and turbulence, respectively. In Eq. (3), $E = h_{\mathrm{sen}} - \frac{P}{\rho_{\mathrm{m}}} + \frac{u_j^2}{2}$, and h_{lat} and h_{sen} represent the latent heat of evaporation and sensible heat, respectively. The first term on the right-hand side of Eq. (3) represents the energy transfer due to conduction.

In previous studies, the realizable *k-ε* model, in which the flow features include strong streamline curvature, vortices, and rotation, has shown substantial improvements over the standard *k-ε* model (Rodio et al., 2012; Lei et al., 2018). So the realizable *k-ε* model is applied.

The flow was simulated with a two-phase model. Vapor phase dispersion is considered homogeneous in the liquid phase, thus the Mixture model was adopted to solve the problem (Jiang et al., 2012). For homogeneous phase model, $\rho_{\mathrm{m}} = \alpha_1\rho_1 + \alpha_{\mathrm{v}}\rho_{\mathrm{v}}$, $u_{\mathrm{m}} = \frac{1}{\rho_{\mathrm{m}}}\left(\alpha_1\rho_1 u_1 + \alpha_{\mathrm{v}}\rho_{\mathrm{v}}u_{\mathrm{v}}\right)$, $\mu_{\mathrm{m}} = \alpha_1\mu_1 + \alpha_{\mathrm{v}}\mu_{\mathrm{v}}$, and $\alpha_1 + \alpha_{\mathrm{v}} = 1$. α is the phase volume fraction, and subscripts l and v mean liquid and gas phases, respectively.

In the cavitation model, the following two-phase continuity equations were used to derive the expression of the mass transfer rate per unit volume R:

For liquid phase:

$$\frac{\partial}{\partial t}\left[\left(1-\alpha_{\mathrm{v}}\right)\rho_1\right] + \nabla\cdot\left[\left(1-\alpha_{\mathrm{v}}\right)\rho_1 u_{\mathrm{m}}\right] = -R; \tag{6}$$

For vapor phase:

$$\frac{\partial}{\partial t}\left(\alpha_{\mathrm{v}}\rho_{\mathrm{v}}\right) + \nabla\cdot\left(\alpha_{\mathrm{v}}\rho_{\mathrm{v}}u_{\mathrm{m}}\right) = R; \tag{7}$$

For mixture:

$$\frac{\partial}{\partial t}\rho_{\mathrm{m}} + \nabla\cdot\left(\rho_{\mathrm{m}}u_{\mathrm{m}}\right) = 0, \tag{8}$$

and

$$\rho_{\mathrm{m}} = \alpha_{\mathrm{v}}\rho_{\mathrm{v}} + \left(1-\alpha_{\mathrm{v}}\right)\rho_1. \tag{9}$$

So the relationship between ρ_{m} and α_{v} is derived:

$$\frac{\mathrm{d}\rho_{\mathrm{m}}}{\mathrm{d}t} = -\left(\rho_1 - \rho_{\mathrm{v}}\right)\frac{\mathrm{d}\alpha_{\mathrm{v}}}{\mathrm{d}t}. \tag{10}$$

The Schnerr-Sauer cavitation model (Zhu, 2018) was applied to calculate α_{v}, which is related to the bubble number density n_{b},

$$\alpha_{\mathrm{v}} = \frac{n_{\mathrm{b}}\frac{4}{3}\pi r_{\mathrm{b}}^3}{1 + n_{\mathrm{b}}\frac{4}{3}\pi r_{\mathrm{b}}^3}, \tag{11}$$

where r_{b} is the radius of the bubble.

The expression of R in general form is:

$$R = \frac{\rho_{\mathrm{v}}\rho_1}{\rho_{\mathrm{m}}}\frac{\mathrm{d}\alpha_{\mathrm{v}}}{\mathrm{d}t}. \tag{12}$$

Combine Eqs. (11) and (12), R is expressed as

$$R = \frac{\rho_{\mathrm{v}}\rho_1}{\rho_{\mathrm{m}}}\alpha_{\mathrm{v}}\left(1-\alpha_{\mathrm{v}}\right)\frac{3}{r_{\mathrm{b}}}\frac{\mathrm{d}r_{\mathrm{b}}}{\mathrm{d}t}. \tag{13}$$

The simplified Rayleigh-Plesset equation is used to account for the time evolution rate of r_{b} as follows (Plesset and Prosperetti, 2003):

$$\frac{\mathrm{d}r_{\mathrm{b}}}{\mathrm{d}t} = \mathrm{sign}\left(P-P_{\mathrm{loc}}\right)\sqrt{\frac{2}{3}\frac{\mathrm{abs}\left\{P-P_{\mathrm{loc}}\right\}}{\rho_1}}, \tag{14}$$

where P_{loc} is the local saturated pressure.

Then R is finally obtained as

$$R = \frac{\rho_{\mathrm{v}}\rho_1}{\rho_{\mathrm{m}}}\alpha_{\mathrm{v}}\left(1-\alpha_{\mathrm{v}}\right)\frac{3}{r_{\mathrm{b}}}\sqrt{\frac{2}{3}\frac{\left(P-P_{\mathrm{loc}}\right)}{\rho_1}}. \tag{15}$$

The value of n_{b} is set as 10^8 according to Zhu et al. (2015), where the simulation results were much consistent with the experimental data with n_{b} of 10^8.

The final equations for the mass transfer of phase change are as follows:

$$R_e = \frac{\rho_v \rho_1}{\rho_m} \alpha_v (1-\alpha_v) \frac{3}{r_b} \sqrt{\frac{2}{3} \frac{(P-P_{loc})}{\rho_1}}, \quad P \geqslant P_{loc}, (16)$$

$$R_c = \frac{\rho_v \rho_1}{\rho_m} \alpha_v (1-\alpha_v) \frac{3}{r_b} \sqrt{\frac{2}{3} \frac{(P_{loc}-P)}{\rho_1}}, \quad P \leqslant P_{loc}, (17)$$

where R_e and R_c account for the mass transfer source terms connected to the growth and collapse of the vapor bubbles, respectively.

2.3 Numerical methodology

The ANSYS Fluent 18.0 was used for the model simulation. The velocity inlet, pressure outlet, and no-slip adiabatic wall were set as the boundary conditions. LN_2 is usually transported with pressurized to 0.2 MPa and subcooled to 77 K in practical transportation. Therefore, the inlet velocity was set as 5 m/s and the outlet pressure was 0.2 MPa of this model. The initial temperatures of the LN_2 and wall were set as 77 K. Besides, physical properties of nitrogen are listed in Table 1. Density, constant-pressure specific heat, and local saturated vapor pressure of LN_2 and vapor nitrogen (VN_2) were specified as the function of temperature. Other physical properties such as the viscosity and thermal conductivity, since their values change little under our working conditions, were set as constants at the condition of 77 K, 0.2 MPa. All the physical data were calculated from Refprop 9.0 developed by National Institute of Standards and Technology (NIST), USA. Pressure-implicit with splitting of operators (PISO) algorithm was adopted to solve the pressure-velocity coupling problem. The time step was set as 10^{-6} s, meeting the convergence requirements of the model at each time step.

2.4 Model verification and grid independence

Since there is no experimental data on cavitation in a cryogenic globe valve, the reliability of the LN_2

cavitation model was verified by its application in the hydrofoil of Hord (1973). The geometry and grid model of this hydrofoil are shown in Fig. 3. The temperature monitoring points are marked in red according to the experiment. The 290 C group in Hord (1973)'s experiment was chosen as the working condition with temperature of 83 K, velocity inlet of 23.9 m/s, pressure outlet, and adiabatic boundary. The calculated pressures and temperatures on the hydrofoil surface were compared with the experimental data in Table 2. The maximum deviations of temperature and pressure are 0.71% and 6.37%, respectively. The simulation results match the experimental data well, and show the validity of the LN_2 cavitation model and its further applicability in the globe valve case.

The grid independence verification of the globe valve model was also carried out with an average grid size/total grid number of 1 mm/175879, 0.8 mm/246288, and 0.5 mm/563764, respectively. With the center of the valve as the origin of the coordinates, monitoring surfaces are set at the valve inlet (s1, $x=$ −115 mm), outlet (s2, x=115 mm), and the downstream pipe (s3−s7, x=200, 300, 400, 500, and 600 mm). Fig. 4 shows the average pressure of each monitored surface under different grids. It is clear that the face-averaged pressures of different positions of grid-246288 and grid-563764 are close to each other, thus the grid-246288 model is acceptable for the further study.

3 Results and discussion

3.1 Field distributions of unsteady LN_2 cavitation in the globe valve

It is observed that the flow fields are basically unchanged in the upstream connecting pipe, the valve upstream and the downstream connecting pipe near the pressure outlet, so these parts are not included in

Table 1 Physical properties of LN$_2$ in simulation

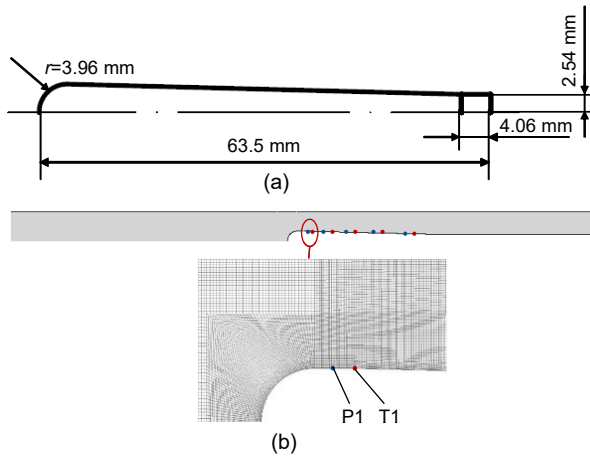| Physical property	Description	
	Liquid nitrogen	Vapor nitrogen
Density (kg/m³)	ρ_1=1161.8−4.5437T	ρ_v=107.847−3.1684T+0.02371T^2
Specific heat (J/(kg·K))	c_{pl}=2381.44−24.93T+0.1868T^2	c_{pv}=2251.93−36.677T+0.2855T^2
Thermal conductivity (W/(m·K))	λ_1=0.145 81	λ_v=7.1458×10³
Viscosity (kg/(m·s))	μ_1=1.635×10⁻⁴	μ_v=5.416×10⁻⁶
Correlation of saturation pressure and temperature	P_v=2885580−84442.4T+626T^2	

Fig. 3 Schematic structure (a) and local grid (b) of the hydrofoil. References to color refer to the online version of this figure

Fig. 4 Grid independence for the cryogenic globe valve model

the following analysis and the area ranging from $x=$ −50 mm to x=300 mm is the main focus of the following discussion for its significant flow and phase change.

Cavitation distribution is characterized in this paper by vapor volume fraction distribution. Fig. 5 shows the vapor volume fraction variations under each opening. It is found that the vapor volume fraction changes periodically under each opening, with periods of about 132, 35, and 7 ms, for the respective openings. The vapor volume fraction under the 33% opening is much higher than those of the other two openings with a vapor volume fraction amplitude of about 0.035, while the amplitude for 100% opening is very small at about $1.5×10^{-5}$.

Figs. 6 – 8 show the typical cavitation distributions in the cryogenic globe valve of LN_2 in a certain period with different openings, where t stands for the initial moment of a certain cavitation period under each opening. As shown in Fig. 6, the vapor occupies a large area and has a high volume fraction under the 33% opening condition, indicating that LN_2 cavitates more readily in the globe valve under that opening. It is observed that the valve chamber is covered with the
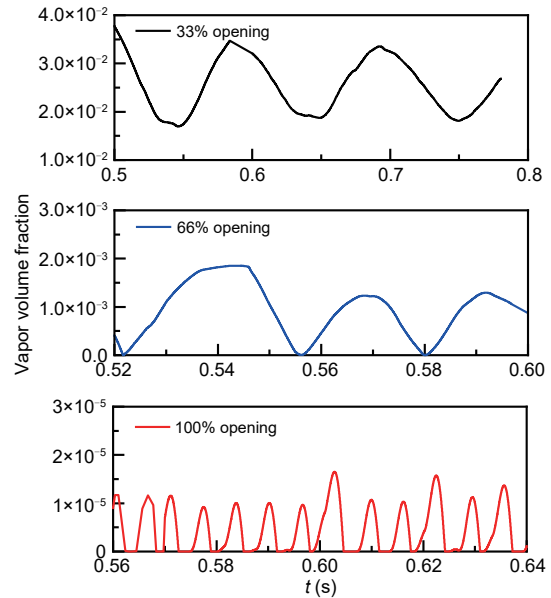

Fig. 5 Vapor volume fraction under various openings of 33%, 66%, and 100%

cavitation cloud during the whole period, with the highest vapor volume fraction above 0.9. It is supposed that since the valve opening is rather small at this time, the throttling effect of the fluid passing through the valve throat is strong enough to generate a large amount of nitrogen gas. It is worth noting that

Table 2 Validation results for the numerical model of the hydrofoil compared to experimental results

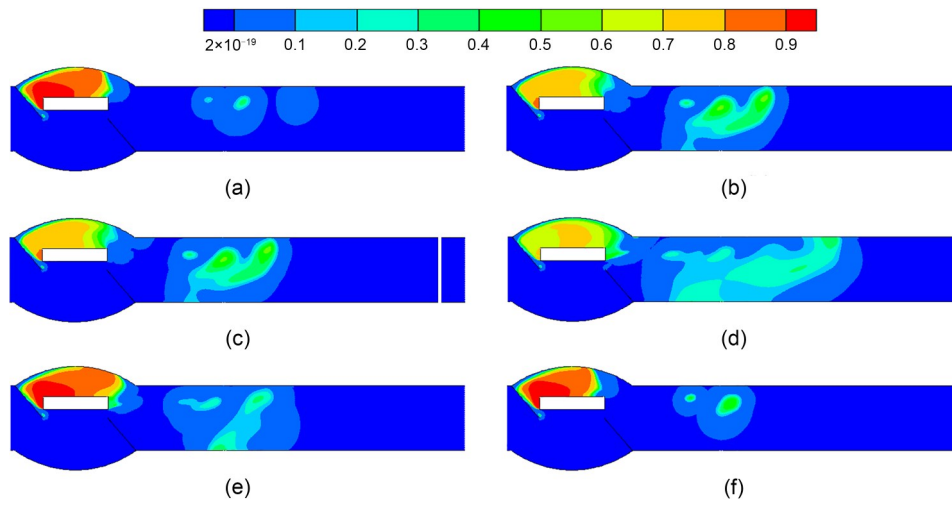| Temperature (K)				Pressure (Pa)			
Position	Experiment (Hord, 1973)	Simulation	Deviation	Position	Experiment (Hord, 1973)	Simulation	Deviation
T1	81.13	80.95	−0.22%	P1	166200	155698	−6.32%
T2	81.53	81.68	0.18%	P2	169000	164310	−2.77%
T3	82.02	82.60	0.71%	P3	177100	177819	0.41%
T4	82.83	83.25	0.51%	P4	346600	368680	6.37%
T5	82.89	83.19	0.36%	P5	383800	369310	−3.78%

Fig. 6 Vapor volume fraction distributions in one period under 33% opening (1 stands for pure gas): (a) *t*; **(b)** *t*+32 ms; **(c)** *t*+43 ms; **(d)** *t*+70 ms; **(e)** *t*+118 ms; **(f)** *t*+133 ms
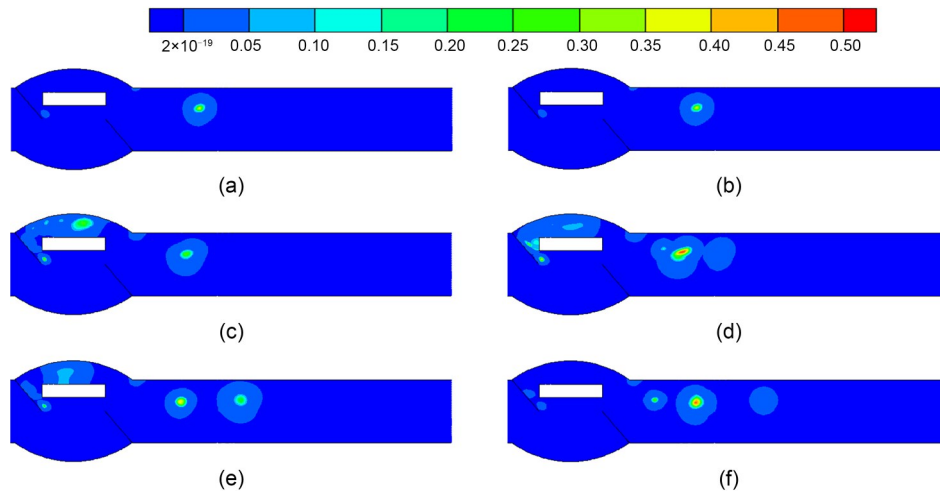

Fig. 7 Vapor volume fraction distributions in one period under 66% opening (1 stands for pure gas): (a) *t*; **(b)** *t*+7 ms; **(c)** *t*+16 ms; **(d)** *t*+20 ms; **(e)** *t*+28 ms; **(f)** *t*+31 ms

the bubbles generated from the valve throat moving downstream make cavitation clouds at the valve downstream, i.e. the cavitation clouds downstream are generated by the throttling effect of the left and right valve throats and are not generated at the valve downstream. It is also observed that at the beginning time *t* of a certain period (Fig. 6a), the downstream pipe contains a low vapor volume fraction, and small bubbles continue to merge and collapse. This state lasts for about 32 ms, and then a larger cavitation cloud forms in the downstream pipe and the merger of the bubbles is still in progress (Fig. 6b). This downstream cavitation cloud keeps growing and when the time reaches *t*+43 ms (Fig. 6c), this cavitation

cloud covers over 70% of the downstream valve area. After that, a much more stable state appears when the cavitation cloud core is deposited at the bottom of the pipe and the cavitation cloud shape is maintained until *t*+70 ms (Fig. 6d). The cavitation cloud area is the maximum at that time for the whole cycle; it includes the valve chamber and the area of the right baffle to the middle of the downstream pipe. The large downstream cavitation cloud then begins to divide into small ones again and merges with the small bubbles continually formed through the right valve throat (Fig. 6e). At the end of this period, the area of the cavitation cloud in the downstream pipe further reduces until it finally returns to the state of time *t* and completes a
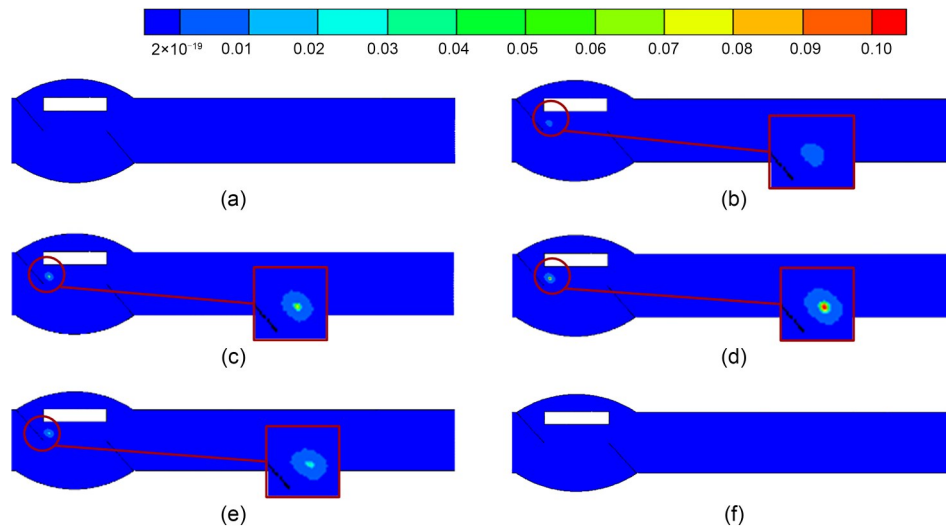
Fig. 8 Vapor volume fraction distributions in a period under 100% opening (1 stands for pure gas): (a) *t*; (b) *t*+1 ms; (c) *t*+2 ms; (d) *t*+5 ms; (e) *t*+6 ms; (f) *t*+7 ms

cavitation period. In a cavitation period of about 133 ms (7.5 Hz), the large cavitation cloud lasts for the longest time, which is about 86 ms (from *t*+32 ms to *t*+118 ms). The development time and collapse time are about 32 ms (from *t* to *t*+32 ms) and 15 ms (from *t*+118 ms to *t*+133 ms), respectively. It should be noted that the cavitation clouds keep merging and collapsing during the whole period, which can produce large pressure oscillations inside the system.

Fig. 7 shows nitrogen cavitation distribution under a valve opening of 66%. The cavitation period is about 31 ms (32.3 Hz), much shorter than the result of 33% opening. Moreover, the maximum vapor volume fraction appears at the downstream bubble core with a value of about 0.5. The bubbles in the downstream pipe continue to merge and rupture and cannot form the same large cavitation cloud as that in the 33% opening due to a much lower vapor volume fraction. As shown in Fig. 7a at time *t*, cavitation clouds can be observed above the left valve throat and in the middle of the downstream pipe. Then bubbles are continually formed and cavitation clouds divide, making the vapor area much bigger, as shown in Fig. 7b. When the time reaches *t*+16 ms (Fig. 7c), the cavitation cloud core forms on the upper surface of the valve core, and there are many small cavitation clouds in the downstream pipe resulting from the original cavitation cloud division. These small cavitation clouds in the downstream pipe further merge, increasing the vapor volume fraction (Fig. 7d). The

cavitation clouds formed in the valve chamber and downstream, keep dividing until time *t*+31 ms (Fig. 7f). The cavitation distribution in the valve chamber is then basically the same as that at the time *t*, completing a cavitation period. The development time, maintenance time, and collapse time of the cavitation clouds in the valve chamber under this opening are about 7, 21, and 3 ms (*t* to *t*+7 ms, *t*+7 ms to *t*+28 ms, and *t*+28 ms to *t*+31 ms), respectively. It is worth noting that the cavitation clouds downstream are also generated from the valve throats under this opening.

When the valve opening reaches 100%, the cavitation phenomenon is very weak, with the maximum vapor volume fraction less than 0.1 as shown in Fig. 8. The cavitation characteristics are mainly reflected in the periodic expansion, shrinkage, and collapse of a small cavitation cloud above the left baffle. The cavitation period is about 7 ms (142.8 Hz) under this opening, which is significantly smaller than those of openings 33% and opening 66%. Owing to the small degree of supercooling of LN_2 in this model, cavitation would still exist even at full opening, while water cavitation does not usually happen at large openings because of its larger supercooling degree at ambient temperature.

As shown in Figs. 6−8, the developing location, the size, and the period of the nitrogen cavitation clouds are totally different under different openings. The extent of valve opening significantly influences the cavitation intensity, which reflects on the local temperature, hydrostatic pressure and fluid flow state. Fig. 9 shows
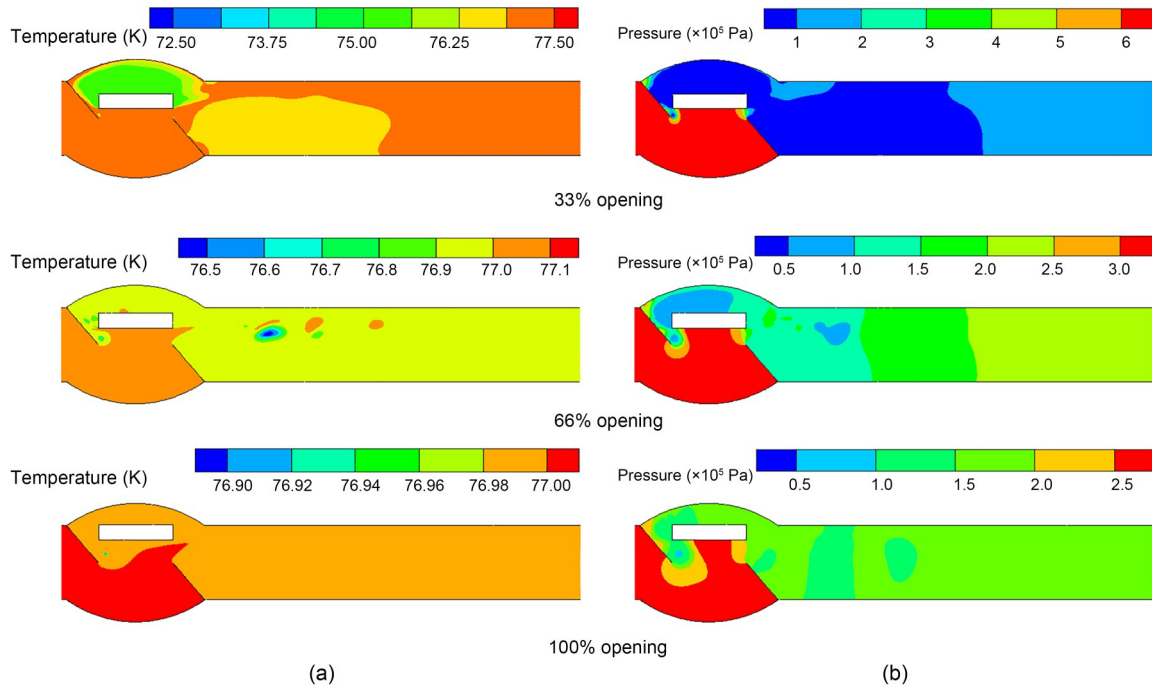
Fig. 9 Temperature distributions (a) and pressure distributions (b) at the maximum vapor volume fraction under each opening

the temperature and pressure distributions of the maximum vapor volume fraction condition under each opening. Local temperature drops and pressure drops at the cavitation clouds are observed with the largest temperature drop being about 5 K under the opening of 33%. The reason is that that fluid pressure reduces significantly after the valve throat, leading to the vaporization of the liquid nitrogen. Due to the latent heat of vaporization, this vaporization process absorbs much heat from the surrounding liquid, resulting in a local temperature drop. In addition, compared to the normal temperature fluids, the lower thermal conductivity of cryogenic liquids will prolong the local temperature drop.

Furthermore, the fluid flow drives the bubbles to move along, causing the cavitation clouds to merge and to separate. Fig. 10 shows the vapor volume fraction and streamline distribution under the conditions of Figs. 6b and 6e; the shape of the cavitation clouds at these two moments is relatively similar. As shown in Fig. 10a, the cavitation cloud core in the downstream pipe overlaps with the vortex core, so the cavitation cloud is maintained for a long time. However, the cavitation cloud core and the vortex core separate obviously in Fig. 10b, so the cavitation cloud splits into small cavitation clouds. In this process, the cavitation

cloud in the valve chamber is also affected by the main flow, for its core moves from the upper surface of the valve core to its left surface. It can be inferred that the surface of the valve core, the baffle, and the downstream pipe are all susceptible of exfoliation by formation and disappearance of bubbles. In addition, due to the large difference in pressure between the two sides of the valve baffles, as shown in Fig. 9b, the resulting torque can easily cause fracture at the bottom of the baffles—especially under the 33% opening.
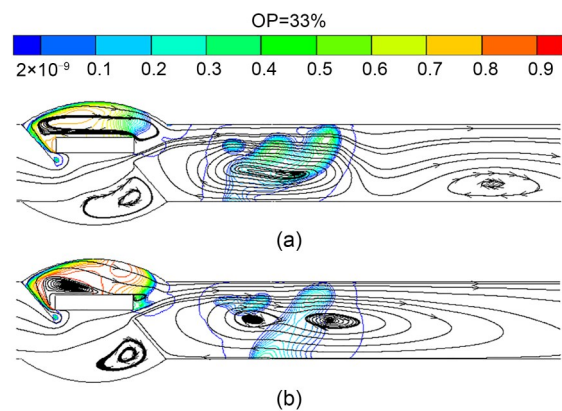

Fig. 10 Vapor volume fraction distribution under 33% opening at *t*+32 ms (a) and streamline distribution under 33% opening (b)

3.2 Wall pressure analysis under various openings

One of the major damages caused by the periodic growth, merge, and collapse of the cavitation bubbles is the transient pressure oscillation in the pipe. The rapid cycle of cavitation leads to a frequent pressure pulse inside. The pressure pulse peak signifies an instantaneous impact on the valve wall, which produces instantaneous huge energy and greatly damages the wall surface, causing wall fatigue and pits. The average pressure refers to the average force on the wall during long time operation, which can be used as a reference for a stiffness and strength check of the material. These two parameters are further investigated later. Monitoring points are set along the wall of the valve and downstream pipe with the most dramatic change in flow characteristics as observed from Figs. 6–8. Locations of monitoring points are shown in Fig. 11, including the bottom of the valve body (p1), the connection part of the valve seat and the valve baffles (p2, p3), the valve chambers (p4, p5), the valve downstream (p6, p7), and the middle of the downstream pipes (p8, p9). Transient pressures of different points over a long periodic operation time are analyzed.

Fig. 12 shows the change of pressure at each monitoring point under 33% opening. The small figures at the top right corner of p1 to p7 are the local, enlarged pictures of pressures at time 0.5–0.8 s (black lines). Comparing the pressures at each monitoring
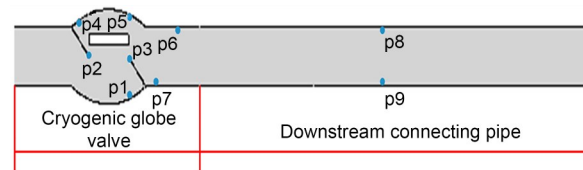

Fig. 11 Monitoring points along the wall surface of cryogenic globe valve and downstream pipe

point (blue lines), the peak values of pressure pulse at p8 and p9 are much larger than those of other monitoring points, and reach 7×10^6 Pa, and the pressure pulse peaks appear more frequently. From the enlarged figures of p1–p7 (black lines), it can be found that the pressures of p1–p7 are also in a periodic pulsation state with the same cycle time of about 130 ms, but their amplitudes are about one order of magnitude smaller than those of p8 and p9. That may be due to the fact that the propagation velocity of a pressure wave in the liquid-gas phase is much smaller than that in the liquid phase (Spalding, 1971). According to Fig. 6, a large volume of cavitation cloud is distributed in the valve chamber and downstream pipe under this opening, which covers points p2–p7. The pressure pulsation of cavitation collapse propagates rapidly in the liquid phase, generating frequent huge pressure pulses at p8 and p9. However, the pressure pulsation of cavitation collapse is damped off by the cavitation clouds in p1–p7, causing the pressure pulsations of p1–p7 to be
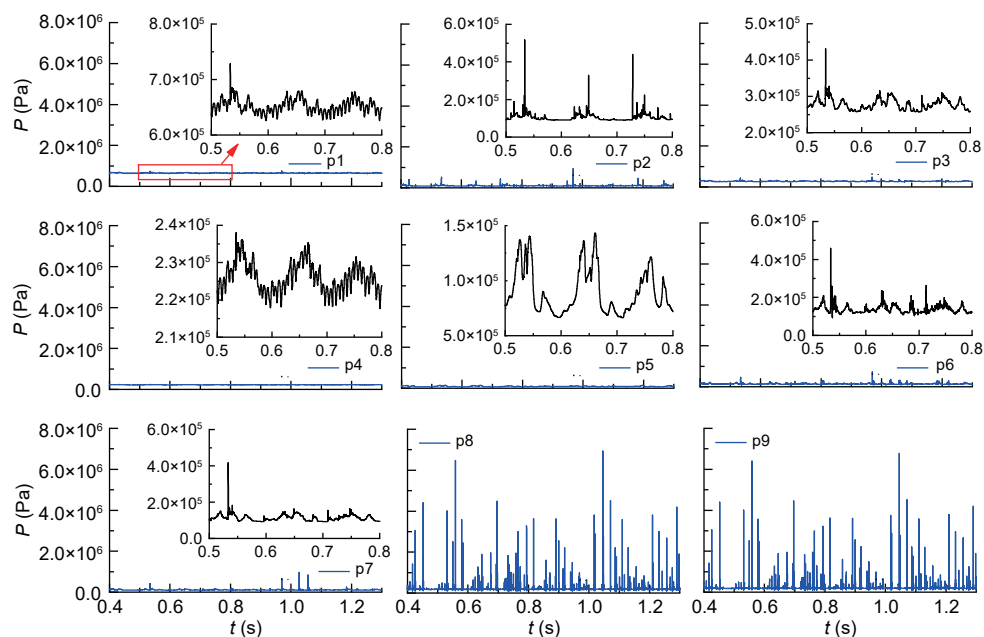

Fig. 12 Pressures of monitoring points under 33% opening. References to color refer to the online version of this figure

much smaller than those of p8 and p9. Comparing the pressure pulsation and average pressure of p1, p8, and p9 which all locate in the liquid area, it is also shown that even though p1 bears the highest average pressure of about 6.5×10^5 Pa during operation, the pressure pulse peaks of p8 and p9 produced by cavitation collapse are much larger than that average pressure of p1. This indicates that the damage risk by cavitation would be much greater than in high working pressure bearing under liquid phase. Besides, the unilateral force downstream from the intense high pressure pulses of p8 and p9 may also cause vibration to the pipeline.

In Watanabe et al. (2008)'s experimental study on the control valve (a similar structure as the model in this paper with twice the diameter), the pulsation frequency of water was about 84.5 Hz with an opening degree of 25% and inlet velocity 2.66 m/s. As stated above, the pressure pulsation frequencies of LN_2 under valve 33% opening are about 7.7 Hz, which is much lower than that of water in valves. Surface tension plays an important role in the expansion and shrinkage of bubbles, by inhibiting their expansion process, and the greater the surface tension of the liquid, the smaller the maximum diameter that the bubble can reach, and thus surface tension accelerates the bubble shrinkage

process. It is noted that the surface tension of water is nearly an order of magnitude larger than that of LN_2, so the collapse period of liquid nitrogen is longer and the pulsation frequency is smaller. Besides, as discussed in Section 3.1, the cavitation process causes a temperature drop and the slope of saturated vapor pressure with temperature of LN_2 is about 10 000 Pa/K while that of water is about 150 Pa/K near the normal working temperature. This means that the cryogenic cavitation causes a local temperature drop, which in turn leads to the rapid drop of local saturated vapor pressure and obviously suppresses the cavitation effect. Therefore, the valve operation of LN_2 transportation should be specifically considered according to its own cavita-tion characteristics.

Fig. 13 shows the nitrogen pressure variations at each monitoring point under 66% opening. They are totally different from those 33% under opening. In Fig. 13, a large pressure pulse peak happens at every monitoring point. The appearance time and values of the pressure pulse peaks at each monitoring point are relatively close. An explanation is that all the monitoring points are in the liquid region under this opening and can spread the instantaneous pressure pulse rapidly, thus making all the monitoring points show a pressure pulse almost simultaneously and have relative
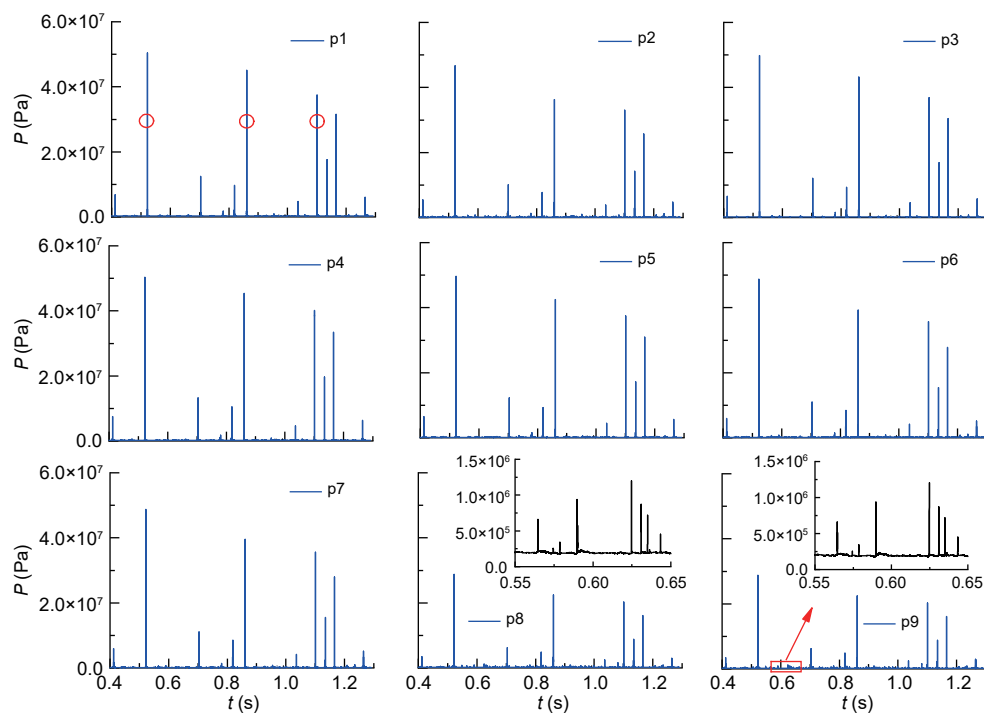

Fig. 13 Monitoring points' pressures under 66% opening

pulse peak values. It is worth noting that the maximum peak value of the pressure pulse here is about 5×10^7 Pa, about 500 times standard atmospheric pressure, which is also about an order of magnitude larger than that of 33% opening. Combined with Fig. 14 which shows the vapor volume fraction distribution at the moments before and after the relatively maximum pressure pulse peaks (as circled in Fig. 13), it is found that obvious bubble clouds are observed before the peak of the pressure pulse, and then disappear after that peak. The collapse of the cavitation clouds is therefore suggested as the reason of the large pressure pulse. Besides, the much bigger value of the pressure pulse peak under 66% opening compare with that of opening 33% may be explained in two ways. Firstly, a large area of cavitation clouds is generated as shown in Fig. 6 under 33% opening, which may cause the energy released by the collapse of bubbles to be damped off by the surrounding bubble clouds. Secondly, the cavitation period of 33% opening (133 ms) is much larger than that in the 66% opening (31 ms), leading to the energy released by the bubble rupture being moderated. Therefore, it can be concluded that the prolonged opening at around 66% should be avoided because of its high risk of fatigue and pits caused by the huge pressure pulse peaks during valve operation.

Besides, it is also found that, different from 33% opening, the peak values of the pressure pulse at p8 and
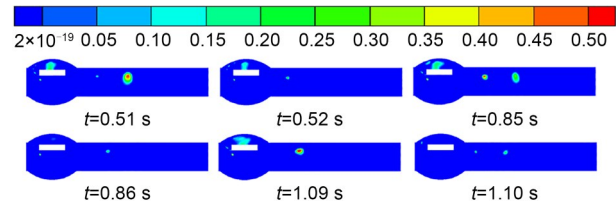

Fig. 14 Vapor volume fraction distribution before and after the appearance of the relative maximum pressure pulse peaks

p9 are smaller than those at p1–p7 in Fig. 13. It is supposed that the cavitation collapse occurs in the region of the valve chamber and valve downstream near the valve body under this condition, so part of the energy has been damped off by the liquid when the pressure pulse reaches p8 and p9, causing the peak values of p8 and p9 to be smaller than those of other points.

Fig. 15 shows the pressure variations under 100% opening. The pressure pulsation is regular under 100% opening, with the maximum pressure pulse peak of about 1.5×10^6 Pa. Similar to the 66% opening, the pressure change at each monitoring point is basically the same, and p8 and p9 have smaller peak values than those of other points. At the same time, the disappearance of the bubbles is also observed before and after the appearance of the maximum pressure pulse peaks under this opening. In addition, because of the extremely low vapor volume fraction, which means the energy released is small when the bubbles burst,
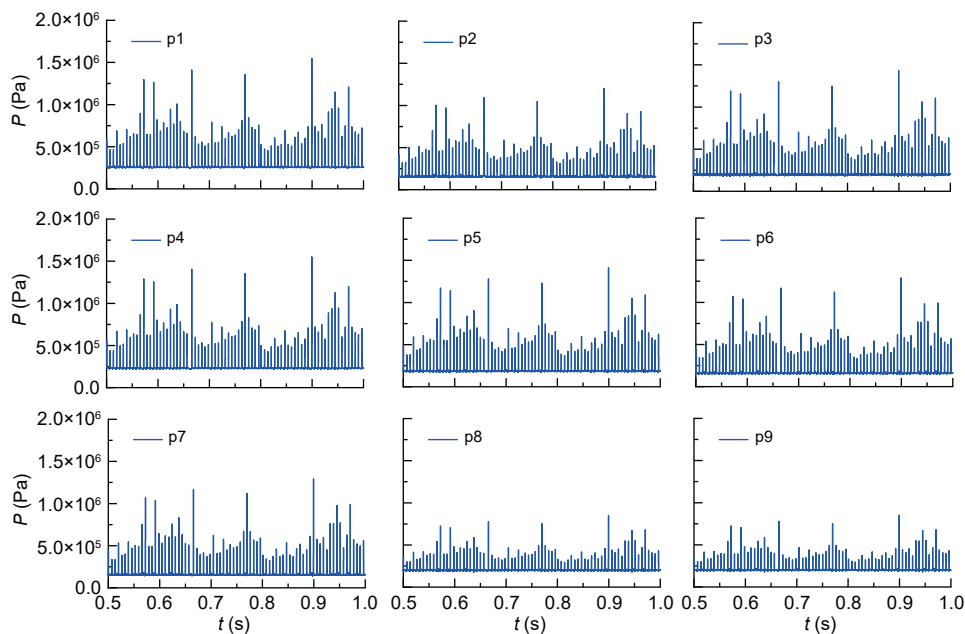

Fig. 15 Pressures of monitoring points p1–p9 under 100% opening

the peak values of the pressure pulse are much smaller under this opening. Besides, there are smaller and more frequent pressure pulse peaks with values and periods of approximately $2.5\times10^5-7.5\times10^5$ Pa and 6.7 ms. Combined with Figs. 13 and 14, it can be summarized that the pressure pulse effect on the valve body and connecting pipe is not only related to the cavitation intensity, but also related to the distributions of gas and liquid.

The durations of the pressure peaks from development to collapse under each opening were also investigated. It is observed that the pressure peak durations are the longest when the opening is 33%, at about 20×10^{-6} s, and some even reach 30×10^{-6} s. When the valve opening reaches 66%, the pressure peak durations maintain about $4\times10^{-6}-6\times10^{-6}$ s, while they are about $6\times10^{-6}-9\times10^{-6}$ s for the valve opening of 100%. That may be the reason that the gas volume fraction is the highest with the valve opening of 33%, thus the external pressure of the cavitation clouds is flattened by the gas, which weakens the collapse process of the bubbles and extends the pressure peak duration. The decrease of the pressure peak duration under openings of 66% and 100% may be due to the obvious decrease of the gas volume fraction and the extrusion of the surrounding liquid. The pressure peak duration of the maximum pressure peak under each opening is shown in Fig. 16.

It is found that compared with the cavitation period of each opening (7–133 ms), the pressure peak collapse can be considered random and its duration as instantaneous, and this is often studied for its instantaneous violent impact on the valve wall. For frequency analysis, the main frequency of the fluid pulsation, namely the cavitation period, is more important and is often investigated to compare it with the natural frequency of the valve system for avoiding vibration resonance.

Fig. 17 shows the average pressure of each monitoring point under various openings. The average pressure of p1 under 33% opening is much higher than that of the other monitoring points under all openings, with a value of about 6.5×10^5 Pa. In addition, the average pressure of p1 is always greater than those of the other monitoring points under each opening. It is supposed that p1 is located in the non-cavitation region that does not experience the throttling and energy dissipation for fluid flow, leading to a much
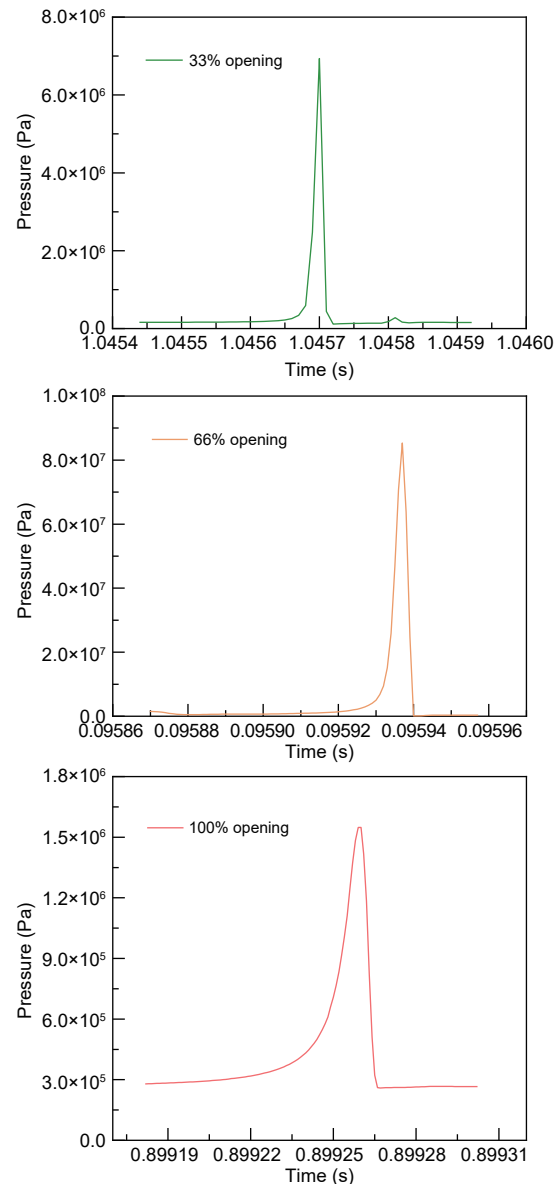

Fig. 16 Pressure peak durations under valve openings of 33%, 66%, and 100%

higher hydrostatic pressure than those at the other points. The change of the average pressure from p1 to other points also shows that the smaller the opening is, the greater the reduction of pressure potential energy after throttling would be. The hydrostatic pressures of the other points are about half of that at point p1 under 33% opening in Fig. 17, i.e. over 50% of the pressure potential energy is converted into kinetic energy and energy dissipation under this condition, which should therefore be avoided in LN_2 practical transportation. In addition, consistent with Fig. 9, the huge average
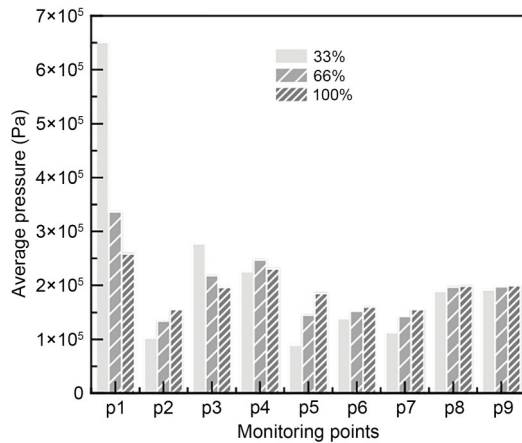
Fig. 17 Average pressures of monitoring points under various openings

pressure difference between p1 and p7 also proves that the bottoms of the baffles are prone to bending or even breaking due to the torque resulting from under 33% opening.

In the above discussions, the average pressure values are far less than the peak values of cavitation pressure pulse. Nevertheless, it should be considered in the stress design of globe valves under the flow of LN_2, especially for the largest average pressure values of locations in upstream non-cavitation areas under small valve opening, such as p1 of 33% opening. Due to the large difference in pressure between the two sides of the valve baffles, the resulting torque can easily cause a fracture at the bottom of the baffles. Besides, vibration can be induced by local pressure pulse in the pipeline under 33% opening for the unilateral force between the upstream non-cavitation area, the valve body, and the downstream intense high pressure pulse area. Meanwhile, the pressure pulses along the whole valve body under openings of 66% are far greater than those under openings of 33% and 100%, and would cause a high risk of fatigue, and pits during the flow of LN_2. Therefore, the valve openings of both 33% and 66% should be avoided for long time operation. The operating conditions of LN_2 associated with its cavitation characteristics under different valve openings should be fully considered in practical valve operation.

3.3 Frequencies analysis

As mentioned above, besides fatigue and pits, another risk caused by cavitation is induced vibration. When the fluid pulsation frequency is close to the valve's natural frequency, vibration resonance will occur and will result in serious vibration problems. It should therefore be avoided (Xu et al., 2017). Fast Fourier transform (FFT) analysis and modal analysis with ANSYS Workbench software (Lawrence, 2012) are applied to observe the fluid pulsation frequencies and the valve system natural frequencies, respectively. FFT is a fast algorithm of discrete Fourier transform (DFT), which transforms data from the time domain to the frequency domain. Here the fluid pulsation frequencies were obtained by FFT analysis on the transient pressures under different valve openings. Modal analysis refers to the natural vibration characteristics of the mechanical structure, including important parameters of specific natural frequency, damping ratio, and mode shape. Fig. 18 shows the mesh model of the cryogenic glove valve with its connecting pipes. Taking account of the actual application, the two ends of the pipes were set to be fixed as the constraint condition. Fig. 19 shows the first-order mode shape of the model with connecting pipe length of 10D. Since both ends of the connecting pipe are fixed, the largest displacement appears at the valve body, which is about 12.4 mm.
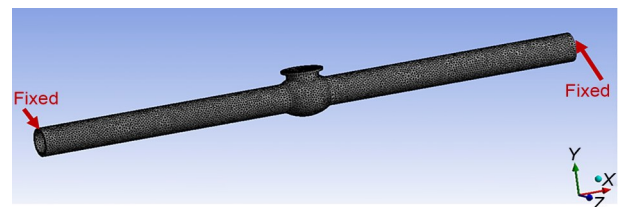

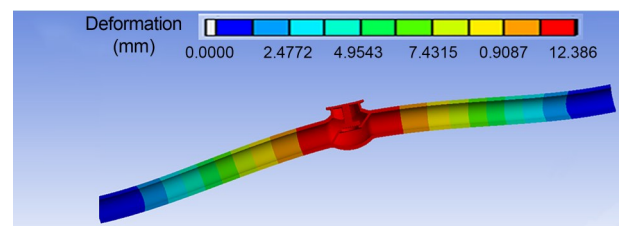**Fig. 18 Mesh of cryogenic glove valve and connecting pipe**

Fig. 19 First-order mode shape of cryogenic globe valve with connecting pipe length of 10D

Furthermore, the natural frequencies of the globe valve with different lengths of connecting pipes were investigated and compared with the fluid pulsation frequencies in Fig. 20. The fluid pulsation frequency increases as the valve opening increases. When the inner diameter and wall thickness of the connecting pipe
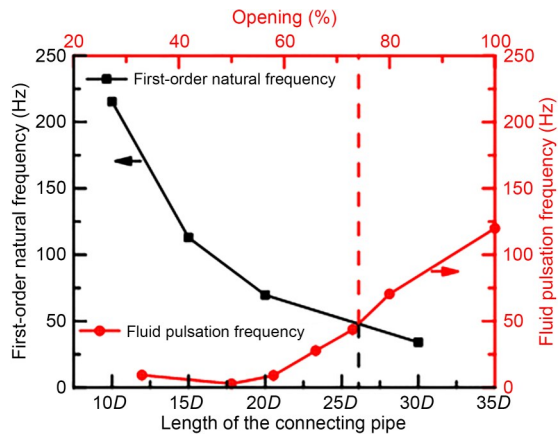
Fig. 20 First-order natural frequency of the valve system with different lengths of connecting pipes and fluid pulsation frequency under different openings

are constant, the first-order natural frequency of the valve system decreases with the increase in length of the connecting pipes. When the valve opening reaches 74%, the fluid pulsation frequency is equal to the natural frequency of the valve system with a connecting pipe length of 26D. Resonance would occur under this condition, which would seriously threaten the safety of operation. The critical point can be used to guide the design of the connecting pipe length.

4 Conclusions

The cavitation characteristics of LN$_2$ in the cryogenic globe valve and associated thermal effects were studied by numerical simulation. The cycle evolution of the cavitation clouds, pressure pulses, and vibration response under different valve openings were investigated. Results are summarized as follows:

1. The LN$_2$ cavitation in the globe valve presents periodical characteristics with periods of 7 ms to 133 ms under different openings. With the increase of the opening, the cavitation period and vapor volume fraction decrease significantly, and the cavitation location changes from the large area at the valve chamber and downstream pipe to the left baffle. With similar valve structure and openings below 33%, the pressure pulsation frequencies of LN$_2$ (10–20 Hz) are lower than those of water (84.5 Hz). Besides, the shape and location of the cavitation clouds are different. The valve operation of LN$_2$ flow should be specifically considered for its own cavitation characteristics.

2. The maximum pressure pulse peak does not occur under the smallest valve opening of 33% with the largest cavitation clouds but appears under the middle opening of 66% with the maximum value reaching 50 MPa, about an order of magnitude larger than those of the 33% and 100% openings. Therefore, in the flow of LN$_2$ through a globe valve, the longtime opening around 66% should be avoided for its high risk of fatigue and pits caused by high pressure pulse peaks. Under an opening of 33%, the peak value and frequency of the instantaneous pressure in the downstream liquid area are very much higher than those of the upstream pipe and the valve body, and would cause not only cavitation impact, but also pipeline vibration. Furthermore, under a small opening, such as 33%, a large pressure difference of about 0.55 MPa will occur between the two sides of the valve baffles, resulting in large torque and high risk of fracture—especially at the bottom of the baffles.

3. The largest displacement of vibration appears at the valve body with both ends of the connecting pipe fixed. In addition, the values of the natural frequency and the fluid pulsation frequency are equal with a connecting pipe length of 26D and a valve opening of 74%. This critical point can be used to guide the design of the connecting pipe length to avoid resonance.

Author contributions

Xia ZHOU designed the research and processed the corresponding data. Xia ZHOU wrote the first draft of the manuscript. Xiao-qin ZHI helped organize the manuscript. Kai WANG and Shao-long ZHU revised and edited the final version. Li-min QIU is the funding acquisition. Xiao-bin ZHANG helped debug the cases in the research. Xu GAO, Yan-yun LIU, and Hong CHEN provided the project administration.

Conflict of interest

Xia ZHOU, Xiao-qin ZHI, Xu GAO, Hong CHEN, Shao-long ZHU, Kai WANG, Li-min QIU, and Xiao-bin ZHANG declare that they have no conflict of interest.

References

Amirante R, Distaso E, Tamburrano P, 2014. Experimental and numerical analysis of cavitation in hydraulic proportional directional valves. *Energy Conversion and Management*, 87:208-219.
https://doi.org/10.1016/j.enconman.2014.07.031

Chen TR, Mu ZD, Huang B, et al., 2021. Dynamic instability analysis of cavitating flow with liquid nitrogen in a converging–diverging nozzle. *Applied Thermal Engineering*, 192:116870.
https://doi.org/10.1016/j.applthermaleng.2021.116870

Chern MJ, Hsu PH, Cheng YJ, et al., 2013. Numerical study on cavitation occurrence in globe valve. *Journal of Energy Engineering*, 139(1):25-34.
https://doi.org/10.1061/(asce)ey.1943-7897.0000084

Comini G, Del Giudice S, 1985. A (k-ε) model of turbulent flow. *Numerical Heat Transfer Applications*, 8(2):133-147.
https://doi.org/10.1080/01495728508961846

Gholami H, Yaghoubi H, Alizadeh M, 2015. Numerical analysis of cavitation phenomenon in a vaned ring-type needle valve. *Journal of Energy Engineering*, 141(4): 04014053.
https://doi.org/10.1061/(asce)ey.1943-7897.0000255

Hord J, 1973. Cavitation in Liquid Cryogens, II-Hydrofoil. NASA Contractor Report, CR-2156, Washington, USA.

Ishimoto J, Kamijo K, 2004. Numerical study of cavitating flow characteristics of liquid helium in a pipe. *International Journal of Heat and Mass Transfer*, 47(1):149-163.
https://doi.org/10.1016/S0017-9310(03)00386-7

Jiang S, Gao H, Sun JS, et al., 2012. Modeling fixed triangular valve tray hydraulics using computational fluid dynamics. *Chemical Engineering and Processing: Process Intensification*, 52:74-84.
https://doi.org/10.1016/j.cep.2011.11.009

Jin ZJ, Gao ZX, Qian JY, et al., 2018. A parametric study of hydrodynamic cavitation inside globe valves. *Journal of Fluids Engineering*, 140(3):031208.
https://doi.org/10.1115/1.4038090

Jin ZJ, Qiu C, Jiang CH, et al., 2020. Effect of valve core shapes on cavitation flow through a sleeve regulating valve. *Journal of Zhejiang University-SCIENCE A (Applied Physics & Engineering)*, 21(1):1-14.
https://doi.org/10.1631/jzus.A1900528

Ko S, Song S, 2015. Effects of design parameters on cavitation in a solenoid valve for an electric vehicle braking system and design optimization. *Journal of Mechanical Science and Technology*, 29(11):4757-4765.
https://doi.org/10.1007/s12206-015-1023-z

Kumagai K, Ryu S, Ota M, et al., 2016. Investigation of poppet valve vibration with cavitation. *International Journal of Fluid Power*, 17(1):15-24.
https://doi.org/10.1080/14399776.2015.1115648

Lee MG, Lim CS, Han SH, 2016. Shape design of the bottom plug used in a 3-way reversing valve to minimize the cavitation effect. *International Journal of Precision Engineering and Manufacturing*, 17(3):401-406.
https://doi.org/10.1007/s12541-016-0050-8

Lei L, Yan H, Zhang HX, et al., 2018. Numerical simulation and experimental research of the flow force and forced vibration in the nozzle-flapper valve. *Mechanical Systems and Signal Processing*, 99:550-566.
https://doi.org/10.1016/j.ymssp.2017.06.024

Li XJ, Shen TJ, Li PC, et al., 2020. Extended compressible thermal cavitation model for the numerical simulation of cryogenic cavitating flow. *International Journal of Hydrogen Energy*, 45(16):10104-10118.
https://doi.org/10.1016/j.ijhydene.2020.01.192

Lin ZH, Li JY, Jin ZJ, et al., 2021. Fluid dynamic analysis of liquefied natural gas flow through a cryogenic ball valve in liquefied natural gas receiving stations. *Energy*, 226: 120376.
https://doi.org/10.1016/j.energy.2021.120376

Miwa S, Mori M, Hibiki T, 2015. Two-phase flow induced vibration in piping systems. *Progress in Nuclear Energy*, 78:270-284.
https://doi.org/10.1016/j.pnucene.2014.10.003

Palau-Salvador G, González-Altozano P, Arviza-Valverde J, 2008. Three-dimensional modeling and geometrical influence on the hydraulic performance of a control valve. *Journal of Fluids Engineering*, 130(1):011102.
https://doi.org/10.1115/1.2813131

Pinho J, Peveroni L, Vetrano MR, et al., 2019. Experimental and numerical study of a cryogenic valve using liquid nitrogen and water. *Aerospace Science and Technology*, 93:105331.
https://doi.org/10.1016/j.ast.2019.105331

Plesset MS, Prosperetti A, 2003. Bubble dynamics and cavitation. *Annual Review of Fluid Mechanics*, 9:145-185.
https://doi.org/10.1146/annurev.fl.09.010177.001045

Rodio MG, de Giorgi MG, Ficarella A, 2012. Influence of convective heat transfer modeling on the estimation of thermal effects in cryogenic cavitating flows. *International Journal of Heat and Mass Transfer*, 55(23-24):6538-6554.
https://doi.org/10.1016/j.ijheatmasstransfer.2012.06.060

Saito S, Shibata M, Fukae H, et al., 2007. Computational cavitation flows at inception and light stages on an axial-flow pump blade and in a cage-guided control valve. *Journal of Thermal Science*, 16(4):337-345.
https://doi.org/10.1007/s11630-007-0337-2

Spalding DB, 1971. One-dimensional two-phase flow: Graham B. Wallis. McGraw-Hill, New York (1969). *International Journal of Heat and Mass Transfer*, 14(8):1229.
https://doi.org/10.1016/0017-9310(71)90219-5

Steckelmacher W, 1994. History and Origins of Cryogenics: Edited by Ralph G Scurlock, Monographs on Cryogenics, Vol. 8. Oxford University Press, Oxford 1992. ISBN 0-19-854814-1, 653 pp. Price £95.00. *Vacuum*, 45(8):919.
https://doi.org/10.1016/0042-207X(94)90134-1

Tabrizi AS, Asadi M, Xie G, et al., 2014. Computational fluid-dynamics-based analysis of a ball valve performance in the presence of cavitation. *Journal of Engineering Thermophysics*, 23(1):27-38.
https://doi.org/10.1134/s1810232814010044

Valdes JR, Rodríguez JM, Monge R, et al., 2014. Numerical simulation and experimental validation of the cavitating flow through a ball check valve. *Energy Conversion and*

Management, 78:776-786.
https://doi.org/10.1016/j.enconman.2013.11.038

Watanabe M, Nshino K, Hagiwara T, et al., 2008. Flow-induced vibration of a control valve in a cavitating flow. *The Proceedings of the Dynamics & Design Conference*, 2008:240-1-240-5.
https://doi.org/10.1299/jsmedmc.2008._240-1_

Xu B, Feng J, Wan FL, et al., 2020. Numerical investigation of modified cavitation model with thermodynamic effect in water and liquid nitrogen. *Cryogenics*, 106:103049.
https://doi.org/10.1016/j.cryogenics.2020.103049

Xu Q, Feng JX, Zhang SC, 2017. Influence of end side displacement load on stress and deformation of "L"-type large-diameter buried pipe network. *Applied Thermal Engineering*, 126:245-254.
https://doi.org/10.1016/j.applthermaleng.2017.07.185

Xue R, Chen L, Zhong X, et al., 2019. Unsteady cavitation of liquid nitrogen flow in spray nozzles under fluctuating conditions. *Cryogenics*, 97:144-148.
https://doi.org/10.1016/j.cryogenics.2018.09.010

Yi DY, Lu L, Zou J, et al., 2015. Interactions between poppet vibration and cavitation in relief valve. *Proceedings of the Institution of Mechanical Engineers Part C: Journal of Mechanical Engineering Science*, 229(8):1447-1461.
https://doi.org/10.1177/0954406214544304

Yu L, Chen H, Gao X, et al., 2019. Simulations on LN_2–VN_2 flooding phenomenon in inclined tubes using a modified AIAD model. *Cryogenics*, 97:100-108.
https://doi.org/10.1016/j.cryogenics.2018.12.002

Zhang XB, Chen JY, Yao L, et al., 2014. Research and development of large-scale cryogenic air separation in China. *Journal of Zhejiang University-SCIENCE A (Applied Physics & Engineering)*, 15(5):309-322.
https://doi.org/10.1631/jzus.A1400063

Zhu JK, 2018. Study on Unsteady Characteristics and Mechanisms of Cryogenic Cavitation. PhD Thesis, Zhejiang University, Hangzhou, China (in Chinese).

Zhu JK, Chen Y, Zhao DF, et al., 2015. Extension of the Schnerr–Sauer model for cryogenic cavitation. *European Journal of Mechanics-B/Fluids*, 52:1-10.
https://doi.org/10.1016/j.euromechflu.2015.01.008

Zhu JK, Zhao DF, Xu L, et al., 2016. Interactions of vortices, thermal effects and cavitation in liquid hydrogen cavitating flows. *International Journal of Hydrogen Energy*, 41(1):614-631.
https://doi.org/10.1016/j.ijhydene.2015.10.042

Zhu SL, Li Y, Zhang RP, et al., 2019. Experimental study on the condensation characteristics of nitrogen with non-condensable gas. *Cryogenics*, 98:29-38.
https://doi.org/10.1016/j.cryogenics.2018.12.007